How to cite: Angew. Chem. Int. Ed. 2024, e202409349
doi.org/10.1002/anie.202409349

Osmotic Energy Conversion Hot Paper

Highly Anion-Conductive Viologen-Based Two-Dimensional Polymer Membranes as Nanopower Generators

Xiaohui Liu[+], Zhiyong Wang[+], Qixiang Zhang[+], Dandan Lei, Xiaodong Li, Zhen Zhang, and Xinliang Feng**

Abstract: Two-dimensional polymers (2DPs) and their layer-stacked 2D covalent organic frameworks (2D COFs) membranes hold great potential for harvesting sustainable osmotic energy. The nascent research has yet to simultaneously achieve high ionic flux and selectivity, primarily due to inefficient ion transport dynamics. This is directly related to ultrasmall pore size (<3 nm), much smaller than the duple Debye length in the diluted electrolyte (6–20 nm), as well as low charge density (<4.5 mC m^{-2}). Here, we introduce a π-conjugated viologen-based 2DP (V2DP) membrane possessing a large pore size of 4.5 nm, strategically enhancing the overlapping of the electric double layer, coupled with an exceptional positive surface charge density (~6 mC m^{-2}). These characteristics enable the membrane to facilitate high anion flux while maintaining ideal selectivity. Notably, V2DP membranes realize an impressive current density of 5.5×10^3 A m^{-2}, surpassing benchmarks set by previously reported nanofluidic membranes. In the practical application scenario involving the mixing of artificial seawater and river water, the V2DP membranes exhibit a considerable ion transference number of 0.70 towards Cl^-, contributing to an outstanding power density of ~55 W m^{-2}. Theoretical calculations reveal the important role of the large quantity of anion transport sites, which act as binding sites evenly located in the positively charged N-containing pyridine rings. These binding sites enable kinematic coupling and decoupling between anions and the V2DP skeleton, establishing a continuous Cl^- ion transport pathway. This work demonstrates the great promise of large-area ultrathin 2DP membranes featuring highly organized charged ion transport networks when applied for osmotic energy conversion.

Introduction

Exploiting renewable and sustainable energy from nature is of paramount importance, especially given the persistent reliance on fossil fuels as well as the growing threat of global warming. A vast reservoir of clean energy exists between river water and seawater, also known as blue energy or osmotic energy.[1–3] This energy source can be harvested through reverse electrodialysis technology by employing ion-selective membranes.[4,5] In recent years, studying two-dimensional (2D) materials as nanofluidic membranes has aroused worldwide interest in osmotic energy harvesting, owing to their potential to overcome the limitations of conventional ion-exchange membranes, such as high resistance.[6–10] Nevertheless, the commonly applied 2D laminar membranes, constructed by stacked thin nanosheets, suffer from elevated resistance caused by the long and zigzag ion transport pathways.[11–14] Encouragingly, ultrathin 2D membranes are emerging as compelling candidates to address this problem. Several pioneering attempts have been made, such as using single-layer MoS_2 with drilled nanopores as osmotic and solar-osmotic power generators.[15–17] However, these membranes are still constrained by low pore density and limited control over pore functionality.

Ultrathin 2D polymers (2DPs) and their layer-stacked 2D covalent organic frameworks (2D COFs) exhibit great superiority owing to their inherent direct ion transport

[*] Dr. Q. Zhang,[+] Dr. D. Lei, Prof. Z. Zhang
Key Laboratory of Precision and Intelligent Chemistry, Department of Applied Chemistry, School of Chemistry and Materials Science, University of Science and Technology of China
Hefei, Anhui 230026 (P. R. China)
E-mail: zhenzhang@ustc.edu.cn

X. Liu,[+] Dr. Z. Wang,[+] Prof. X. Feng
Center for Advancing Electronics Dresden & Faculty of Chemistry and Food Chemistry,
Technische Universität Dresden
01069 Dresden (Germany)
E-mail: xinliang.feng@tu-dresden.de

Dr. Z. Wang,[+] Dr. X. Li, Prof. X. Feng
Department of Synthetic Materials and Functional Devices,
Max Planck Institute of Microstructure Physics, Weinberg 2, Halle 06120 Germany

Dr. Q. Zhang,[+] Dr. D. Lei, Prof. Z. Zhang
Suzhou Institute for Advanced Research,
University of Science and Technology of China
Suzhou, Jiangsu 215123 (P. R. China)

[+] These authors contributed equally to this work.

channels and designable building blocks.[18–20] However, existing studies have struggled to achieve both large ion flux and high selectivity simultaneously due to the inefficiency of the ion transport process. This inefficiency stems from an incomplete understanding of the relationship between the channel geometry, charge density, and membrane performance. In the ideal case, the channel diameter should closely match the duple Debye screening length, leading to an extremely unipolar ionic environment. The counterions will be the dominant charge carriers and concentrate inside the nanochannels, substantially enhancing the ionic conductivity compared to the bulk conditions. In the osmotic energy harvesting process, the duple Debye length of the charged surface in the low concentration side (1–10 mM) falls within the range of 6–20 nm, which appears much larger than the investigated 2DP membranes' pore sizes (<3 nm). Therefore, it would greatly compromise the ionic flux when the previous strategies monotonously focus on minimizing pore size down to nanometer or even sub-nanometer scale. Meanwhile, reported 2DP membranes generally suffer from insufficient charge density, resulting in low ion selectivity.[18,21,22] Given this intricate interplay, constructing large-area 2DP membranes with highly charged surfaces and smartly designed channels is imperative for enhancing the ion transport properties comprehensively.

In this work, we demonstrate a fully crystalline viologen-based 2DP (V2DP) membrane capable of simultaneously achieving high ionic flux and selectivity. This V2DP membrane with a thickness of ~35 nm and a great positive charge density (~6 mC m^{-2}), possesses abundant nanoscale ion transport channels (~5.8×10^{16} m^{-2}). Especially, the precisely tailored pore size of 4.5 nm could enable electric double layer overlap and also ensure large ion flux concurrently. Leveraging these structural advancements, V2DP membranes demonstrate exceptional anion transport capabilities, realizing an impressive current density of 5.5×10^{3} A m^{-2}, a significant improvement over previously reported anion transport nanofluidic membranes. Furthermore, when mixing artificial seawater and river water, the V2DP membranes achieve a substantial transference number of 0.70 towards Cl^- ions and a remarkable power density of 55 W m^{-2}, outperforming most reported 1D and 2D anion transport membranes. Density functional theory (DFT) and molecular dynamics (MD) simulations underscore the working role of the abundant binding sites located within positively charged pyridine rings on the V2DP backbones. These binding sites enable kinematic coupling and decoupling between the viologen units and ions, forming a continuous and efficient Cl^- ion transport pathway with a low energy barrier. This study unveils the immense potential of large-area 2DP membranes with highly ordered and charged ion transport networks, showcasing their possibilities in propelling the frontier of sustainable energy generation.

Results and Discussion

Fully Crystalline Viologen-Based 2DP (V2DP) Membrane

The V2DP membranes, featuring adequate and efficient anion transport space, were synthesized using the surfactant monolayer-assisted interfacial synthesis strategy (Figure 1a, Figure S1 and Methods in Supporting Information).[19] The synthesis involved the Schiff-base polycondensation between positively charged monomer **1** (1,1′-bis(4-aminophenyl)-[4,4′-bipyridine]-1,1′-diium chloride) and monomer **2** (2,4,6-trihydroxybenzene-1,3,5-tricarbaldehyde) on the water surface. Fourier transform infrared spectra demonstrated the disappearance of the characteristic absorption peaks of $-NH_2$ groups from monomer **1** and the –CHO groups from monomer **2**, indicating the efficient conversion of amine and aldehyde groups into imine linkages (Figure S2). Following the polymerization under trifluoromethanesulfonic acid condition, the counter-ions (Br^-) within the viologen units were replaced by $CF_3SO_3^-$ ions, as evidenced by the X-ray photoelectron spectroscopy results (Figure S3). The resultant membrane with shiny reflection, exhibited optical uniformity and robustness that allows for transfer onto desired substrates such as SiO_2/Si wafer and transmission electron microscopy (TEM) grid (Figure 1b and Figure S4–S5). Meanwhile, the V2DP membranes have great scalability, their sizes can be synthesized from 28 cm^2 to 113 cm^2 as displayed in Figure S6. Atomic force microscopy (AFM) image demonstrates a nanoscale thin thickness of ~35 nm (Figure 1c), which can be potentially tuned by varying the monomer concentration and reaction time. The selected-area electron diffraction (SAED) pattern displays a diffraction ring at 0.22 nm^{-1}, indicating that the V2DP membrane is polycrystalline with a pore size of ~4.5 nm (Figure 1d inset). High-resolution TEM (HRTEM) image shows periodic hexagonal pores (~4.5 nm), showcasing full crystallinity with domain sizes ranging from 50 to 100 nm (Figure 1d).

By nanoindentation testing, the mechanical strength of V2DP membranes was measured **(**Figure 1e). The Young's modulus can achieve as high as 7.6 GPa, superior to pure Kevlar membrane.[23] A hardness of about 0.6 GPa was obtained, which is better than many high-strength polymers such as isotactic polypropylene (~0.13 GPa) and high-density polyethylene (~0.06 GPa) (Figure 1f). With excellent strength, the V2DP membrane manifests its great potential for osmotic energy conversion. Moreover, the V2DP membrane exhibits a positively charged backbone with a high spatial density of cationic sites (8.8×10^{7} m^{-3}), which would contribute to the selective anion transport phenomenon. To further understand this, a continuum-based 2D Poisson-Nernst-Planck (PNP) model is employed to simulate the V2DP channel (Figure S7). As demonstrated in Figure 1g, the ion distribution inside the V2DP channel is predicted, in which anion concentration is much larger than the cation concentration along the radial direction, confirming the anion transport potential of the V2DP membrane.[24,25]

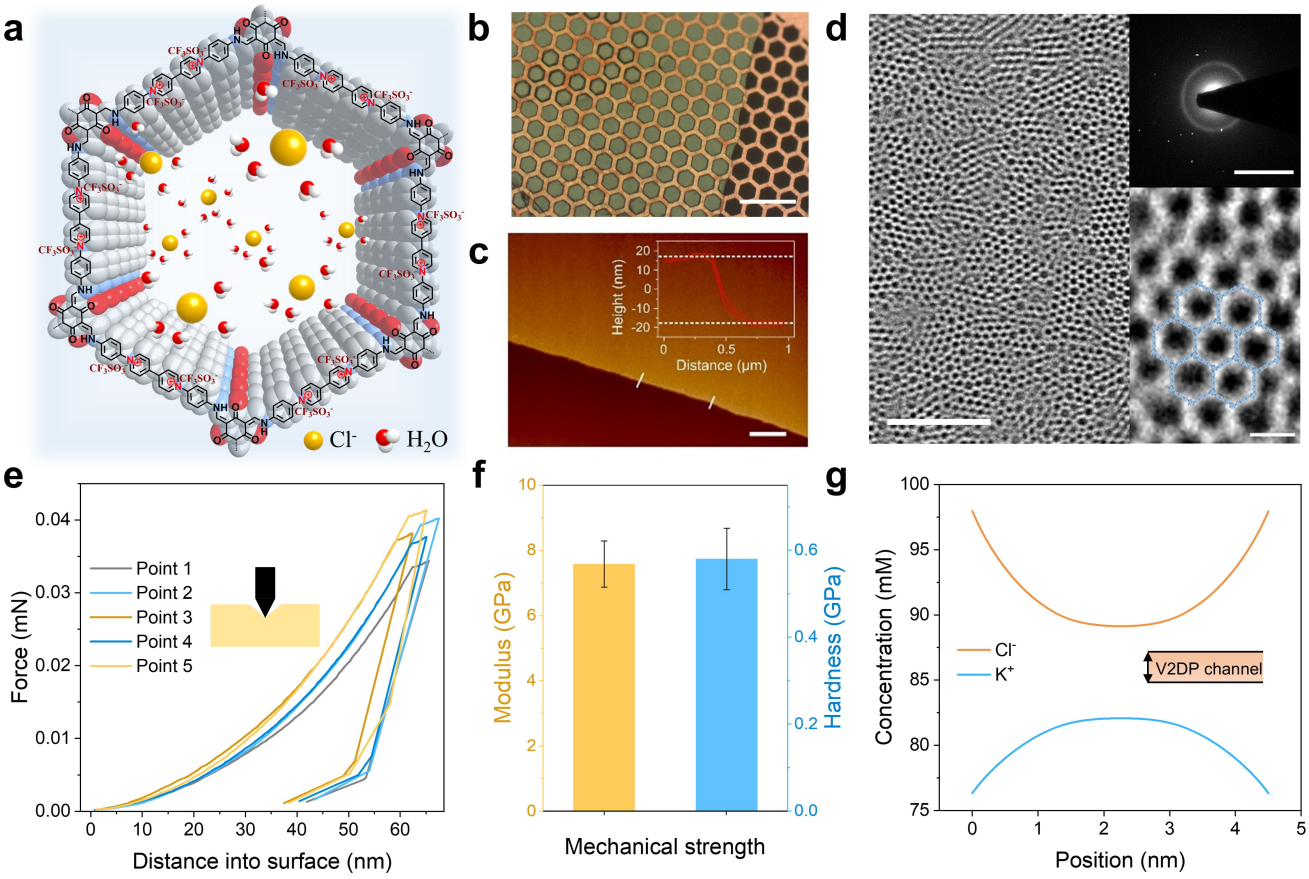

Figure 1. Fully crystalline viologen-based 2DP (V2DP) membrane. (a) Chemical structure of the highly anion-conductive V2DP membrane. (b) Optical image of the V2DP membrane transferred onto a Cu grid (scale bar: 100 μm). (c) AFM image of the V2DP membrane (scale bar: 100 nm). Inset, the profiles of the section marked by white lines. (d) HRTEM and FFT of the V2DP in different magnified zone (scale bar: left, 50 nm, right top: 0.5 nm^{-1}, right bottom: 5 nm). (e) The load-displacement curve of V2DP in nanoindentation testing. (f) Modulus and hardness of the V2DP membrane. (g) Calculated concentration of anion (Cl^-) and cation (K^+) along the V2DP channel under a 0.1/0.01 M KCl concentration gradient.

Electric-Potential-Driven Ion Transport

To investigate the ion transport behaviour, the V2DP membrane was first transferred onto a silicon wafer with a single hole in the center, then mounted between a two-compartment electrochemical cell (Figure 2a and Figure S8–S9). Figure 2b shows the *I–V* curves of the V2DP membrane recorded under symmetric KCl electrolyte conditions. Different from the separate silicon hole (Figure S10), the current in the negative bias is much larger than that measured in the positive bias. Such a non-linear ion transport behaviour is the so-called ionic diode that resembles the rectification effect in semiconducting p–n junction, which can be ascribed to the intrinsic positive charged nature of the V2DP membrane.[26,27] The charged V2DP membranes and the uncharged conical Si hole are combined as asymmetric channels with asymmetric geometry and charge density (Figure 2c). Such junction between a charged zone and a neutral zone formed a unipolar diode, which possesses a typical ion rectification phenomenon. When the positive voltage bias is applied, the depletion zone forms between the charged tip (V2DP membranes) and the neutral base (Si hole). Consequently, the current is reduced and the ion rectification phenomenon occurs.[28,29] The transmembrane conductance is proportional to the concentration at high KCl concentrations and starts to deviate from the linear dependence at ~10^{-1} M, which is a signature of the existing surface charge within the membrane (Figure 2d).[30] Then, we evaluated the surface charge density of V2DP by fitting the conductance data with the existing conductance model.[31] The use of a constant surface charge model results in a significant deviation from the measured values. Therefore, the surface charge is not constant but should depend on the ion concentration. By assuming a variable model, the surface charge density is estimated to be ~1 $mC m^{-2}$ at 0.001 M and ~6 $mC m^{-2}$ at 0.1 M, which is higher than the reported ZnTPP-COF monolayer, black phosphorus, graphene oxide, and boron nitride nanosheets (less than 4.5 $mC m^{-2}$).[13,18,31,32]

The pH is found to have a remarkable influence on the ionic diode effect of V2DP membranes, as shown in Figure 2e. The rectification ratio decreases from 2.7 to 2.6, then to 1.8 upon increasing pH from 3 to 11, indicating the decreasing surface charge density, especially in the alkaline solution. The influence of various halogen electrolytes is also investigated in Figure 2f: the V2DP membrane exhibits

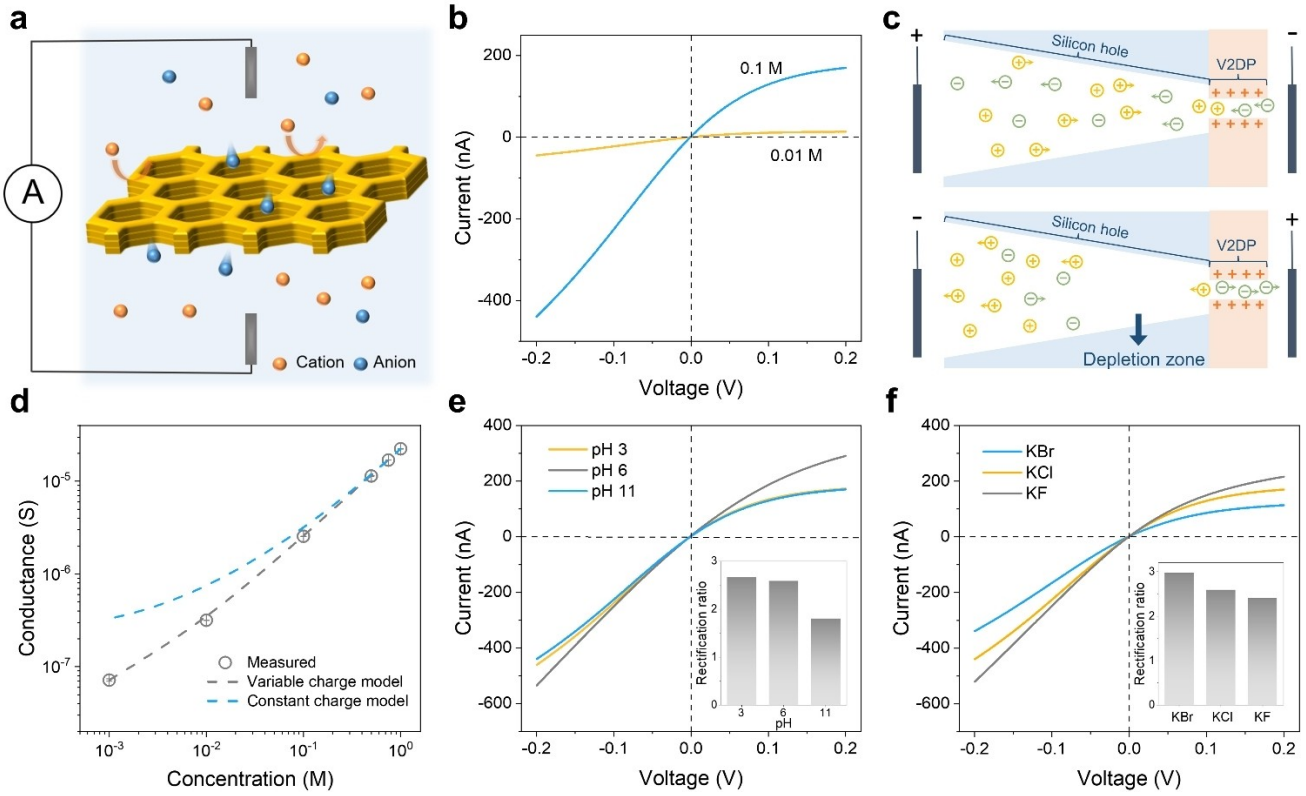

Figure 2. Electric-potential-driven ion transport. (a) Schematic of the ion transport measurement across the membrane. (b) *I–V* curve of the V2DP membrane recorded under KCl electrolyte of different concentrations. (c) Illustration of operation of unipolar diode formed by positively charged V2DP and neutral silicon hole at negative voltage bias (top) and positive voltage bias (bottom). (d) Transmembrane ionic conductance of the V2DP membrane as well as the theoretical fit by assuming variable (black) and constant (blue) charge model. (e, f) Influence of the pH (e) and electrolyte type (f) on the ion transport process.

the highest rectification ratio in the KBr electrolyte (3.0) and the lowest in the KF electrolyte (2.4), according to their mobility trend ($F^- < Cl^- < Br^-$).[33]

Selective Anion Transport and Osmotic Energy Conversion

Because of the high density of vertically oriented channels (5.8×10^{16} m^{-2}) and well-defined cationic sites, the V2DP membrane is capable of efficiently conducting anions, shedding light in osmotic energy conversion under a transmembrane concentration gradient. Figure 3a shows the *I–V* curve of the V2DP membranes recorded under 0.1/0.01 M KCl concentration gradient. Obvious intercepts are observed on the x/y axis, which is the so-called osmotic current (I_{os}) and osmotic voltage (V_{os}).[34] The redox potential generated by the unequal voltage on the electrode has been offset by using a pair of saturated potassium chloride salt bridges.[35] As the concentration gradient increases, the V_{os} first increases from 27 to 37 mV, and then decreases to 33 mV (Figure 3a, inset and Figure S11). The weakened osmotic potential is due to the decrease in thickness of electric double layer as concentration increases.[36–38] The transference number is also reducing as the V_{os} decreases, but it still can achieve a fair value around 0.7 even at 50-fold, because the pore size of 4.5 nm is still enough for the overlap of the electric double layer with length of 3.1 nm at low concentration side (Methods and Table S1 in Supporting Information).[23,39,40] Nevertheless, the I_{os} keeps increasing as the gradient increases, and the V2DP membranes deliver a great current density of 4.6×10^3 $A\,m^{-2}$ at 50-fold since it has a fully crystalline structure as well as a high spatial density of positively charged sites.

We also found that the V_{os} and I_{os} are electrolyte-dependent (Figure S12), where V_{os} shows a monotonous decrease from KF to KBr (40 mV to 36 mV). This can be ascribed to the decreasing charge density of anions, which will weaken the interaction between anions and V2DP skeleton (Figure 3b). I_{os} of KCl and KBr are the same (20 nA) and I_{os} of KF is the lowest (14 nA), due to the combined effect of ion mobility ($F^- < Cl^- < Br^-$) and the charge density ($F^- > Cl^- > Br^-$). Specifically, Cl^- and Br^- can move faster and have less interaction with V2DP due to the lower charge density, but F^- moves slower and interacts strongly with V2DP. As a result, the osmotic power density ($P_{max} = V_{os}\times I_{os}$) of 16 $W\,m^{-2}$ under a 10-fold KCl concentration gradient is the highest (Figure 3c). We also investigated the influence of the cation type, including K^+, Na^+, and Li^+. As shown in Figure 3d, both the I_{os} and V_{os} increase as the mobility of the cation decreases (Figure S13) because the decreased mobility will enhance the anion-cation separation efficiency.[27] Consequently, under a 50-fold concentra-

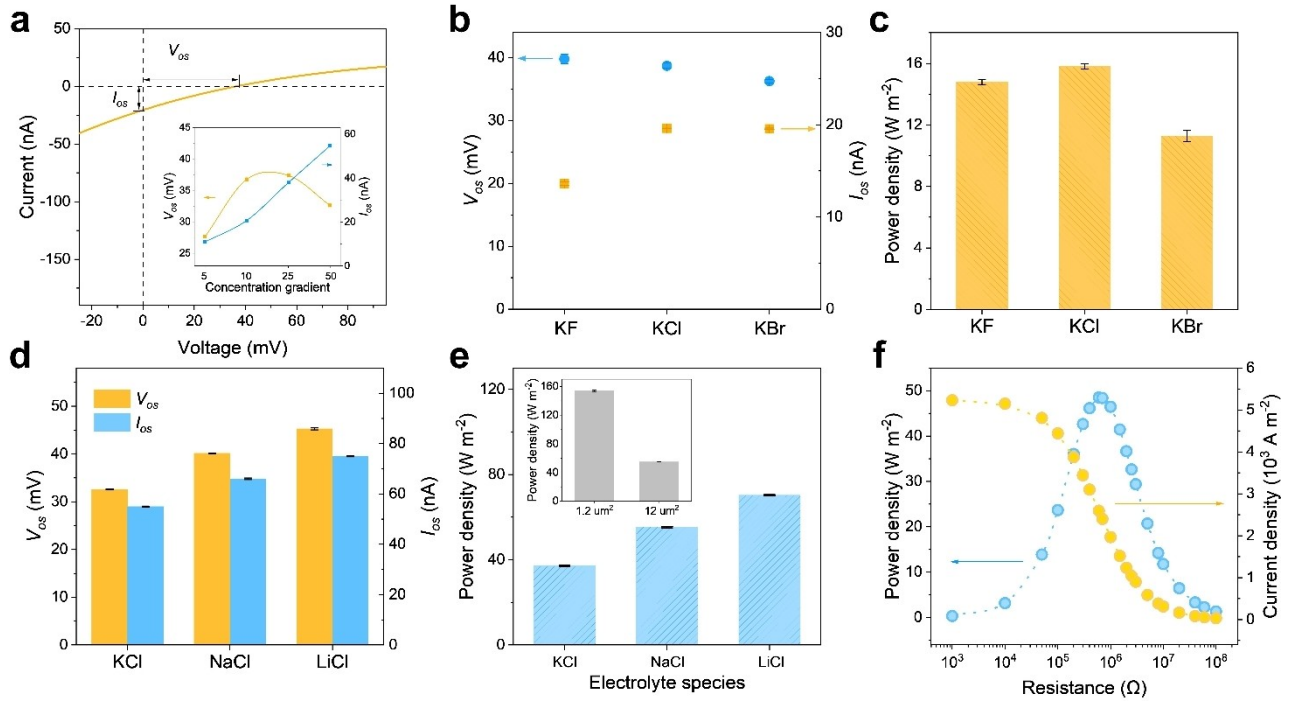

Figure 3. Selective anion transport and osmotic energy conversion. (a) *I–V* curve of the V2DP membrane recorded under 10-fold KCl (0.1/0.01 M) concentration gradient. The inset shows the variation of I_{os} and V_{os} as a function of the transmembrane concentration gradient. (b) Influence of the different anion electrolytes on the measured I_{os} and V_{os}. (c) The V2DP membrane exhibits the highest power density of about 16 W m^{-2} in KCl electrolyte (10-fold concentration gradient). (d) Influence of the different cation electrolytes on the measured I_{os} and V_{os} (50-fold concentration gradient). (e) The V2DP membrane exhibits the highest power density about 70 W m^{-2} in LiCl electrolyte (50-fold concentration gradient). (f) The collected power can be transferred to the external circuit to supply an electronic load. The output power density can achieve about 48.5 W m^{-2}.

tion gradient, KCl obtained the lowest P_{max} of 37 W m^{-2} and LiCl realized the highest P_{max} of about 70 W m^{-2} (Figure 3e). Under 50-fold NaCl as artificial seawater and river water, the P_{max} of V2DP membranes can achieve about 55 W m^{-2}, mainly owing to an impressive improvement of the ion conductivity (current density of 5.5×10^3 A m^{-2}) over previously reported anion-selective membranes (Table S3).[22,26,41–45] When the testing area is reduced to 1.2 μm^2, there is a slight increase in anion selectivity, accompanied by a substantial boost in current density to 1.55×10^4 A m^{-2}. This enhancement contributes to a great P_{max} of ~155 W m^{-2}, outperforming most of the state-of-the-art 1D and 2D membranes (Figure S14, Table S2 and Table S3).[46–48] Such a high-power output can be ascribed to the lower penetrating resistance, fewer grain boundaries, and fewer stochastic defects in the sub-microscale device.[49] In addition, the power density shows a decrease upon increasing the membrane thickness due to the considerable reduction of I_{os} in thicker membranes, highlighting the benefits of this thickness-adjustable membrane (Figure S15). As predicted, the V_{os} and I_{os} of the V2DP membrane are both pH dependent and undergo significant decreases upon changing the pH of NaCl electrolytes from 3 to 11 (testing area: 12 μm^2) (Figure S16). The power density obtained at pH 3 is about 58 W m^{-2} due to the abundant positive sites, including the inherent positive N in pyridine rings and the protonated N in the imine bond. At pH 11, the power density is about 38 W m^{-2} because of the increasing electronegativity of ketone oxygens, which would weaken the positively charged property of V2DP (Figure S17). The harvested osmotic power can be output to an external circuit.[41,50] As the resistance increases, the current density decreases, and the power density, calculated by $P_{out}=I^2\times R_0$, achieves a maximum value of about 48.5 W m^{-2} at 0.6 MΩ as exhibited in Figure 3f (testing area: 12 μm^2). In addition, the performance of V2DP under mixed salt solution (including Na^+, Mg^{2+}, Ca^{2+}, Cl^- and SO_4^{2-}) was also measured (Figure S18). Both ion flux and selectivity improved compared to that of 0.5/0.01 M NaCl. The power density realized a higher value of 67 W m^{-2} than the 55 W m^{-2} of pure NaCl electrolytes, owing to the increased Cl^- quantity and the lower diffusion coefficient of divalent cations.[18,51]

Identify the Active Sites of V2DP Membranes

To elucidate the active sites of the V2DP membrane during energy conversion, we synthesized neutral 2DP (N2DP) as a contrast sample employing neutral monomer **1** ([1,1′:4′,1″:4″,1‴-quaterphenyl]-4,4‴-diamine) instead of the viologen-based monomer (Figure 4a and **Methods** in Supporting Information). In FTIR spectra, the vanishing peaks of $-NH_2$ groups in monomer **1** and –CHO groups in monomer **2** confirm the successful synthesis of the N2DP membranes (Figure S19). Under a 10-fold KCl concentration gradient and at pH 6, N2DP obtains different V_{os} (−5 mV)

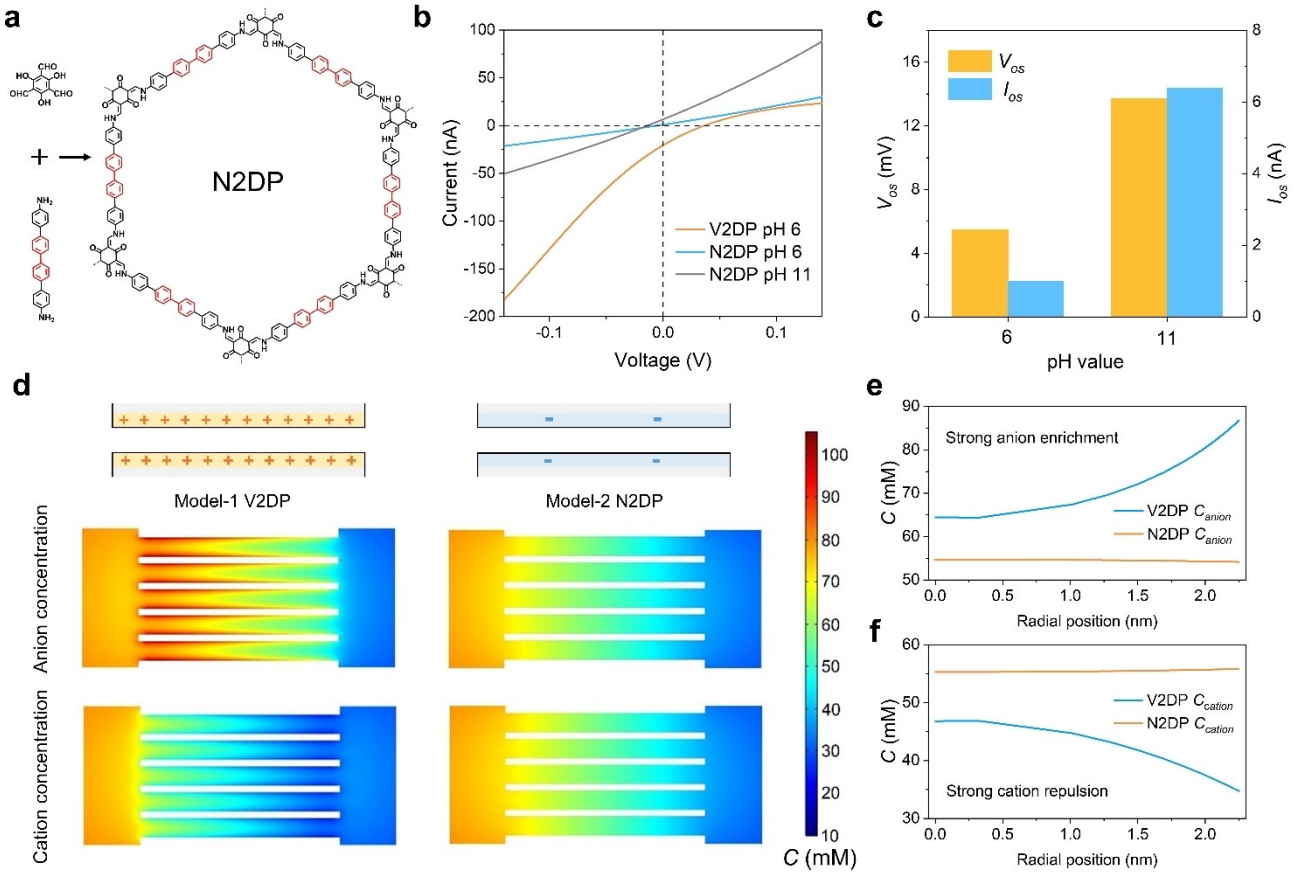

Figure 4. Identify the active sites. (a) Synthesis of the contrast sample N2DP with neutral monomer **1**. (b) *I–V* curve of the N2DP membrane recorded under 10-fold KCl concentration gradient (0.1/0.01 M) of different pH values. *I–V* curve of the V2DP membrane recorded under pH 6 is also plotted for a direct comparison. (c) V_{os} and I_{os} of the N2DP membrane under different pH values. (d) Calculated cation and anion concentration of simulated V2DP channel (model 1) and N2DP channel (model 2) under equilibrium using PNP equations. (e) Radial distribution of anion and cation in simulated V2DP channel and N2DP channel, indicating the strong exclusion and enrichment effect (EEE) of the V2DP membrane.

and I_{os} (1 nA) from the V_{os} (36 mV) and I_{os} (−20 nA) of V2DP. These results indicate that N2DP exhibits cation selectivity in contrast to V2DP's anion selectivity (Figure 4b). With increasing pH, the V_{os} and I_{os} of the N2DP membrane improve to −14 mV and 6 nA, respectively (Figure 4c). The power density of the V2DP membrane is only 0.1 and 2 $W m^{-2}$ at pH 6 and pH 11, respectively, much lower than the 16 $W m^{-2}$ of the V2DP membrane (Figure S20). These findings demonstrate that the positively charged pyridine rings and the electronegative ketone oxygens both serve as the charging unit in V2DP membranes. They play a competitive role in the overall ion selectivity as well as the energy conversion process, which is in line with the pH-dependent performance.

Continuum-based simulations were performed to provide deeper insights into the selective ion diffusion process. Two types of nanochannel arrays with different charge densities (+6 $mC m^{-2}$ and −0.2 $mC m^{-2}$) were built to resemble the inherent nanochannels of V2DP and N2DP membranes, respectively. Figure 4d shows the distribution of anions and cations under a steady regime. Unlike the N2DP channel, the local anion concentration within the V2DP channel exhibits non-uniformity. The extension of the electric double layer results in a gradual increase in the counterion concentration from the channel's center to its surface. For cations, the scenario is conversed and the corresponding concentration distribution exhibits a reverse shape. Notably, the ionic radial distribution profiles reveal a strong exclusion and enrichment effect (EEE) of the V2DP membrane (Figure 4e–f). The concentration of anion is much higher than that of cation, attributed to the enhanced electrostatic interaction of the ions with V2DP channel. In essence, the transport pathway of anions through the V2DP channel is electrostatically "widened", while conversely, the transport pathway of cations is electrostatically "narrowed", thus yielding excellent anion selectivity. It is noteworthy that the enrichment effect also substantially augments the number of anions in the V2DP channel available for transport via diffusion, thereby contributing to higher ionic flux.

Molecular Insight

To investigate the ion diffusion mechanism across the V2DP membrane, density functional theory (DFT) calculations were employed. We first established a single-layer V2DP structure model, as shown in Figure 5a. In the V2DP model structure, there are two types of positions where ions can be readily adsorbed, namely on the pyridine rings containing positively charged N (A-site) and on the carbonyl groups (B-site). Figure 5b shows the adsorption energies of these two types of sites for Cl^- and K^+ ions, which are about −2.2 eV (A-site, Cl^-), −1.7 eV (B-site, Cl^-), −0.7 eV (A-site, K^+) and −2.0 eV (B-site, K^+). At the A-site, the adsorption locations of the Cl^- and K^+ are different, which is also revealed by the differential charge density map (Figure S21). Due to the strongly positively charged nature of the pyridine rings, Cl^- tend to be adsorbed on the charged part of pyridine ring, while K^+ are more likely to be adsorbed in the middle of the two charged pyridine rings. The carbonyl group in the B-site includes partially positively charged C and partially negatively charged O, which leads to the adsorption of both Cl^- and K^+ (Figure S22). Overall, the Cl^- ion tends to adsorb at A-sites, while K^+ preferentially interact with B-sites. The ion migration pathway and energy barrier of K^+ and Cl^- across the V2DP structure are studied as shown in Figure 5c–d, elaborately illustrating the efficient anion selectivity mechanism of V2DP. During the ion migration process, Cl^- ions tend to jump from one adsorption site to another adjacent adsorption site. Observed from electrostatic potential (ESP), the positive charge not only center at the N but also continuously distributed on the whole V2DP backbones. This extensive charge distribution provide more charged sites for the interaction with anions, enabling efficient ion transport (Figure S22). Thus, the Cl^- ions exhibit a low energy barrier (0.64 eV) and can migrate quickly with high throughput. In contrast, K^+ ions are repelled by the positively charged N during migration and adsorbed to the carbonyl group. This adsorption-repulsion-adsorption migration process results in a larger barrier (1.94 eV) and a resistant migration path of K^+ than that of Cl^-. Molecular dynamics (MD) simulations present the ion movement process, with snapshots taken at 0 and 3 ns. The top view exhibits the kinematic coupling and decoupling between the V2DP backbones and Cl^- ions, showing the formation of a continuous Cl^- transport pathway (Figure 5e–f). In contrast, K^+ are repelled by the positive pyridine rings and located at the center of the nanochannel, indicating that K^+ cannot undergo continuous transport through the adsorption sites on the V2DP backbone. This observation is consistent with the results from DFT calculations. Consequently, Cl^- ions can migrate much

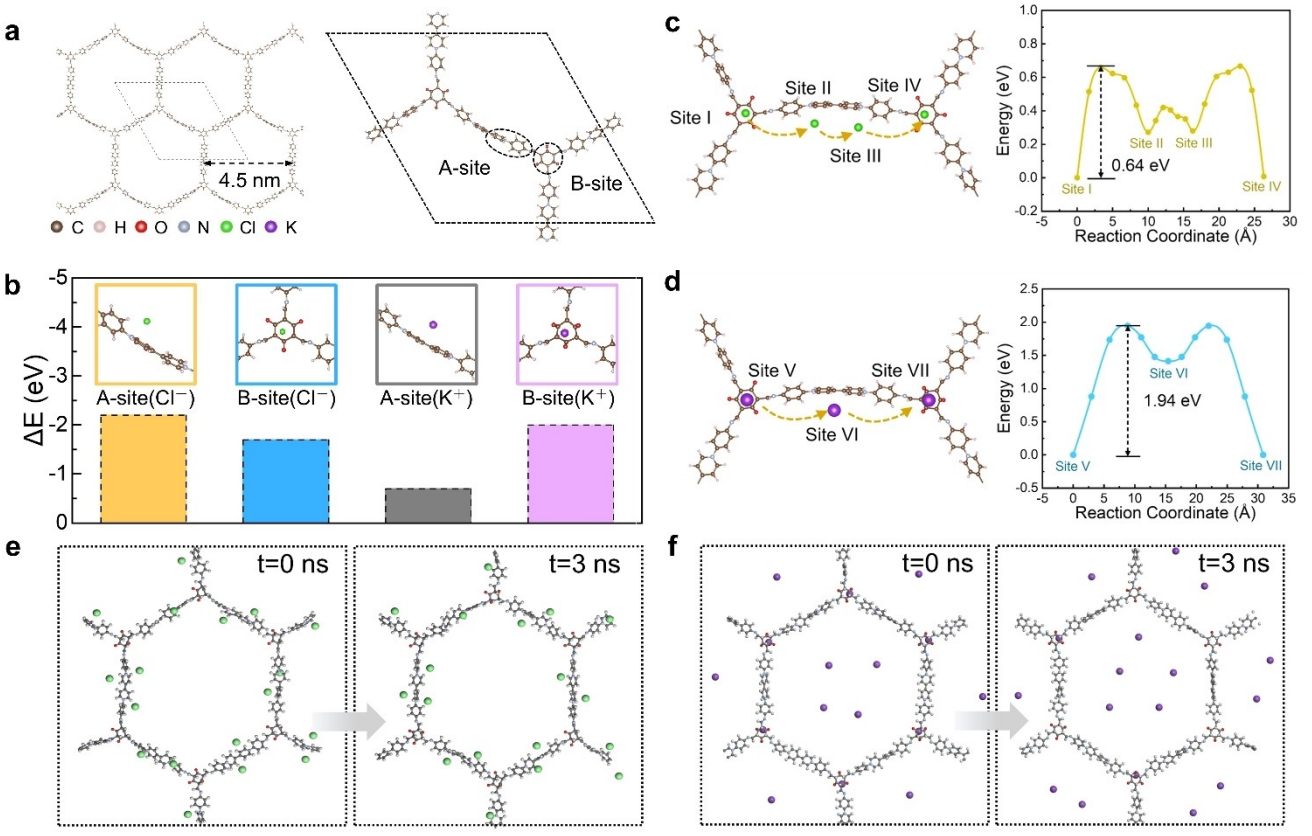

Figure 5. Molecular insight. (a) Single-layer V2DP structure model used for density functional theory (DFT) calculations. (b) Calculated adsorption energies of A- and B- sites for Cl^- and K^+ ions. (c, d) Ion migration pathway and energy barrier across the V2DP model structure, (c) Cl^- ion, (d) K^+ ion. (e, f) Molecular dynamics (MD) of ion movement process across the V2DP model structure, (e) Cl^- ion, (f) K^+ ion.

easier across V2DP than K^+, ultimately realizing the efficient anion selectivity of V2DP.

Conclusion

In summary, we present a fully crystalline viologen-based 2DP membrane with tailored pore size and high charge density for high-performance osmotic energy conversion. By facilitating efficient anion transport dynamics, V2DP membranes exceptionally overcome the trade-off between ionic flux and selectivity. The transference number achieves a substantial value of 0.70 for Cl^-, which is considerable for the large pore size (~4.5 nm) of V2DP. Upon mixing artificial seawater and river water, V2DP membranes realize a remarkable current density of 5.5×10^3 A m^{-2} and superior power density of up to 55 W m^{-2}, outperforming the performance of most anion-selective membranes. Both experiments and simulations validate the presence of abundant positively charged anion binding sites distributed on the V2DP backbones, forming a continuous anion transport pathway and reducing the anion transport energy barrier, hence realizing the high anion transport efficiency.

Acknowledgements

This work was financially supported by the European Union's Horizon 2020 research and innovation programme under grant agreement No 881603, the European Science Foundation (ESF), and the Coordination Networks: Building Blocks for Functional Systems (SPP1928, COORNET), CRC1415, ERC Grants on T2DCP and FC2DMOF (No. 852909), and the Leading Talents of Innovation and Entrepreneurship of Gusu District (ZXL2023341). Open Access funding enabled and organized by Projekt DEAL.

Conflict of Interest

The authors declare no conflict of interest.

Data Availability Statement

The data that support the findings of this study are available from the corresponding author upon reasonable request.

Keywords: 2D polymer · nanofluidics · ion transport · osmotic energy conversion

[1] S. Chu, A. Majumdar, *Nature* **2012**, *488*, 294–303.
[2] A. Siria, M.-L. Bocquet, L. Bocquet, *Nat. Chem. Rev.* **2017**, *1*, 0091.
[3] X. Tong, S. Liu, J. Crittenden, Y. Chen, *ACS Nano* **2021**, *15*, 5838–5860.
[4] A. Zlotorowicz, R. V. Strand, O. S. Burheim, Ø. Wilhelmsen, S. Kjelstrup, *J. Membr. Sci.* **2017**, *523*, 402–408.
[5] Z. Fang, Y. Dong, Z. Guo, Z. Zhao, Z. Zhang, Z. Liang, H. Yao, *Appl. Phys. A* **2022**, *128*, 1080.
[6] W. Xin, L. Jiang, L. Wen, *Acc. Chem. Res.* **2021**, *54*, 4154–4165.
[7] M. Macha, S. Marion, V. V. R. Nandigana, A. Radenovic, *Nat. Rev. Mater.* **2019**, *4*, 588–605.
[8] A. Esfandiar, B. Radha, F. C. Wang, Q. Yang, S. Hu, S. Garaj, R. R. Nair, A. K. Geim, K. Gopinadhan, *Science* **2017**, *358*, 511–513.
[9] X. Chen, Y.-B. Zhu, H. Yu, J. Z. Liu, C. D. Easton, Z. Wang, Y. Hu, Z. Xie, H.-A. Wu, X. Zhang, D. Li, H. Wang, *J. Membr. Sci.* **2021**, *621*, 118934.
[10] K. Fan, S. Zhou, L. Xie, S. Jia, L. Zhao, X. Liu, K. Liang, L. Jiang, B. Kong, *Adv. Mater.* **2024**, *36*, 2307849.
[11] Z. Zhang, S. Yang, P. P. Zhang, J. Zhang, G. B. Chen, X. L. Feng, *Nat. Commun.* **2019**, *10*, 2920.
[12] A. R. Koltonow, J. Huang, *Science* **2016**, *351*, 1395–1396.
[13] S. Qin, D. Liu, G. Wang, D. Portehault, C. J. Garvey, Y. Gogotsi, W. Lei, Y. Chen, *J. Am. Chem. Soc.* **2017**, *139*, 6314–6320.
[14] L. Ding, D. Xiao, Z. Lu, J. Deng, Y. Wei, J. Caro, H. Wang, *Angew. Chem. Int. Ed.* **2020**, *59*, 8720–8726.
[15] J. Feng, M. Graf, K. Liu, D. Ovchinnikov, D. Dumcenco, M. Heiranian, V. Nandigana, N. R. Aluru, A. Kis, A. Radenovic, *Nature* **2016**, *536*, 197–200.
[16] L. Wang, M. S. H. Boutilier, P. R. Kidambi, D. Jang, N. G. Hadjiconstantinou, R. Karnik, *Nat. Nanotechnol.* **2017**, *12*, 509–522.
[17] D. Pakulski, W. Czepa, S. D. Buffa, A. Ciesielski, P. Samorì, *Adv. Funct. Mater.* **2020**, *30*, 1902394.
[18] J. Yang, B. Tu, G. Zhang, P. Liu, K. Hu, J. Wang, Z. Yan, Z. Huang, M. Fang, J. Hou, Q. Fang, X. Qiu, L. Li, Z. Tang, *Nat. Nanotechnol.* **2022**, *17*, 622–628.
[19] K. Liu, H. Qi, R. Dong, R. Shivhare, M. Addicoat, T. Zhang, H. Sahabudeen, T. Heine, S. Mannsfeld, U. Kaiser, Z. Zheng, X. Feng, *Nat. Chem.* **2019**, *11*, 994–1000.
[20] S. Jiang, L. Meng, W. Ma, G. Pan, W. Zhang, Y. Zou, L. Liu, B. Xu, W. Tian, *Mater. Chem. Front.* **2021**, *5*, 4193–4201.
[21] Z. Wang, Z. Zhang, H. Qi, A. Ortega-Guerrero, L. Wang, K. Xu, M. Wang, S. Park, F. Hennersdorf, A. Dianat, A. Croy, H. Komber, G. Cuniberti, J. J. Weigand, U. Kaiser, R. Dong, X. Feng, *Nat. Synth.* **2022**, *1*, 69–76.
[22] X. Liu, X. Li, X. Chu, B. Zhang, J. Zhang, M. Hambsch, S. C. B. Mannsfeld, M. Borrelli, M. Löffler, D. Pohl, Y. Liu, Z. Zhang, X. Feng, *Adv. Mater.* **2024**, *36*, 2310791.
[23] C. Chen, G. Yang, D. Liu, X. Wang, N. A. Kotov, W. Lei, *Adv. Funct. Mater.* **2022**, *32*, 2102080.
[24] H. S. White, A. Bund, *Langmuir* **2008**, *24*, 2212–2218.
[25] J. Wang, M. Zhang, J. Zhai, L. Jiang, *Phys. Chem. Chem. Phys.* **2014**, *16*, 23–32.
[26] X. Zhu, J. Hao, B. Bao, Y. Zhou, H. Zhang, J. Pang, Z. Jiang, L. Jiang, *Sci. Adv.* **2018**, *4*, eaau1665.
[27] J. Lu, H. Zhang, J. Hou, X. Li, X. Hu, Y. Hu, C. D. Easton, Q. Li, C. Sun, A. W. Thornton, M. R. Hill, X. Zhang, G. Jiang, J. Z. Liu, A. J. Hill, B. D. Freeman, L. Jiang, H. Wang, *Nat. Mater.* **2020**, *19*, 767–774.
[28] Z. S. Siwy, S. Howorka, *Chem. Soc. Rev.* **2010**, *39*, 1115–1132.
[29] X. Huang, X.-Y. Kong, L. Wen, L. Jiang, *Adv. Funct. Mater.* **2018**, *28*, 1801079.
[30] W. Kong, C. Wang, C. Jia, Y. Kuang, G. Pastel, C. Chen, G. Chen, S. He, H. Huang, J. Zhang, S. Wang, L. Hu, *Adv. Mater.* **2018**, *30*, 1801934.
[31] S. Hong, C. Constans, M. V. Surmani Martins, Y. C. Seow, J. A. Guevara Carrió, S. Garaj, *Nano Lett.* **2017**, *17*, 728–732.
[32] Z. Zhang, P. Zhang, S. Yang, T. Zhang, M. Löffler, H. Shi, M. R. Lohe, X. Feng, *Proc. Natl. Acad. Sci. USA* **2020**, *117*, 13959–13966.

[33] S. Koneshan, J. C. Rasaiah, R. M. Lynden-Bell, S. H. Lee, *J. Phys. Chem. B* **1998**, *102*, 4193–4204.
[34] C.-Y. Lin, C. Combs, Y.-S. Su, L.-H. Yeh, Z. S. Siwy, *J. Am. Chem. Soc.* **2019**, *141*, 3691–3698.
[35] S. Garaj, W. Hubbard, A. Reina, J. Kong, D. Branton, J. A. Golovchenko, *Nature* **2010**, *467*, 190–193.
[36] M. A. Brown, A. Goel, Z. Abbas, *Angew. Chem. Int. Ed.* **2016**, *55*, 3790–3794.
[37] C. Wang, J. Tang, L. Li, J. Wan, Y. Ma, Y. Jin, J. Liu, H. Wang, Q. Zhang, *Adv. Funct. Mater.* **2022**, *32*, 2204068.
[38] R. Qu, X. Zeng, L. Lin, G. Zhang, F. Liu, C. Wang, S. Ma, C. Liu, H. Miao, L. Cao, *ACS Nano* **2020**, *14*, 16654–16662.
[39] C. Chen, D. Liu, L. He, S. Qin, J. Wang, J. M. Razal, N. A. Kotov, W. Lei, *Joule* **2020**, *4*, 247–261.
[40] Z. Zhang, S. Yang, P. Zhang, J. Zhang, G. Chen, X. Feng, *Nat. Commun.* **2019**, *10*, 2920.
[41] Y.-C. Liu, L.-H. Yeh, M.-J. Zheng, K. C. W. Wu, *Sci. Adv.* **2021**, *7*, eabe9924.
[42] Z. Zhang, X. Sui, P. Li, G. Xie, X.-Y. Kong, K. Xiao, L. Gao, L. Wen, L. Jiang, *J. Am. Chem. Soc.* **2017**, *139*, 8905–8914.
[43] Z. Wang, Z. Zhang, H. Qi, A. Ortega-Guerrero, L. Wang, K. Xu, M. Wang, S. Park, F. Hennersdorf, A. Dianat, A. Croy, H. Komber, G. Cuniberti, J. J. Weigand, U. Kaiser, R. Dong, X. Feng, *Nat. Synth.* **2021**, *1*, 69–76.
[44] J. Xiao, M. Cong, M. Li, X. Zhang, Y. Zhang, X. Zhao, W. Lu, Z. Guo, X. Liang, G. Qing, *Adv. Funct. Mater.* **2024**, *34*, 2307996.
[45] Z. Zhang, X.-Y. Kong, K. Xiao, Q. Liu, G. Xie, P. Li, J. Ma, Y. Tian, L. Wen, L. Jiang, *J. Am. Chem. Soc.* **2015**, *137*, 14765–14772.
[46] H. Wang, L. Su, M. Yagmurcukardes, J. Chen, Y. Jiang, Z. Li, A. Quan, F. M. Peeters, C. Wang, A. K. Geim, S. Hu, *Nano Lett.* **2020**, *20*, 8634–8639.
[47] X. Liu, M. He, D. Calvani, H. Qi, K. B. S. S. Gupta, H. J. M. De Groot, G. J. A. Sevink, F. Buda, U. Kaiser, G. F. Schneider, *Nat. Nanotechnol.* **2020**, *15*, 307–312.
[48] Z. Man, J. Safaei, Z. Zhang, Y. Wang, D. Zhou, P. Li, X. Zhang, L. Jiang, G. Wang, *J. Am. Chem. Soc.* **2021**, *143*, 16206–16216.
[49] Z. Zhang, P. Bhauriyal, H. Sahabudeen, Z. Wang, X. Liu, M. Hambsch, S. C. B. Mannsfeld, R. Dong, T. Heine, X. Feng, *Nat. Commun.* **2022**, *13*, 3935.
[50] G. Laucirica, M. E. Toimil-Molares, C. Trautmann, W. Marmisollé, O. Azzaroni, *Chem. Sci.* **2021**, *12*, 12874–12910.
[51] Z. Huang, M. Fang, B. Tu, J. Yang, Z. Yan, H. G. Alemayehu, Z. Tang, L. Li, *ACS Nano* **2022**, *16*, 17149–17156.

Manuscript received: May 17, 2024
Accepted manuscript online: July 4, 2024
Version of record online: ■■, ■■

Research Article

Osmotic Energy Conversion

X. Liu, Z. Wang, Q. Zhang, D. Lei, X. Li, Z. Zhang,* X. Feng* **e202409349**

Highly Anion-Conductive Viologen-Based Two-Dimensional Polymer Membranes as Nanopower Generators

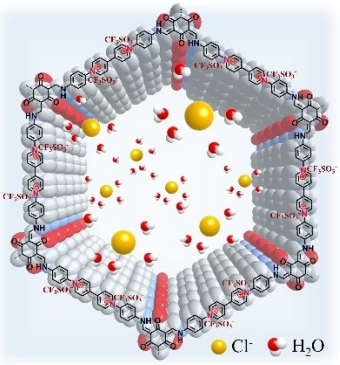

We developed a fully crystalline viologen-based 2DP (V2DP) membrane that can simultaneously achieve high ionic flux and selectivity, possessing great positive charge density and abundant ion transport nanochannels. Benefitting from the tailored pore size of 4.5 nm, it demonstrates an impressive current density of 5.5×10^3 A m^{-2} and maintains a substantial anion selectivity of 0.70, as a result, it realizes a remarkable power density of 55 W m^{-2}.